9.3 Transonic Flows

Contributed by:
M. Raffel, J. Kompenhans

Common problems appearing in the application of PIV at high flow velocities in wind tunnels are limited optical access and problems of focusing the images of the tracer particles due to vibrations and density gradients in the flow [60]. Nevertheless, the instantaneous flow fields above a helicopter blade profile and in the wake of a model of a cascade blade have been investigated successfully at transonic flow velocities by means of the photographic PIV technique already a decade ago [310].

Today, PIV can be applied to transonic flows in industrial wind tunnels, such as the DNW-TWG with a cross-section of $1 \times 1\,\mathrm{m}^2$, even on a routine basis. Modern model deformation measurement techniques allow for the determination of the exact model location and deformation under load in parallel with the measurement of the instantaneous flow fields. Furthermore, the simultaneous application of Pressure Sensitive Paints (PSP) and PIV improves our understanding of the complex flow field, for example over delta wings in the transonic regime. Thus, PIV – in combination with PSP or deformation measurements – provides high quality data for the validation of numerical codes (see section 9.8).

Table 9.7. PIV recording parameters for cascade flow.

Flow geometry	$Ma = 1.27$ parallel to light sheet
Maximum in-plane velocity	$U_{\max} \approx 400\,\mathrm{m/s}$
Field of view	$150 \times 100\,\mathrm{mm}^2$
Interrogation volume	$2.8 \times 2.8 \times 1\,\mathrm{mm}^3$ $(H \times W \times D)$
Dynamic spatial range	DSR $\approx 57 : 1$
Dynamic velocity range	DVR $\approx 100 : 1$
Observation distance	$z_0 \approx 1\,\mathrm{m}$
Recording method	single frame/double exposure
Ambiguity removal	image shifting/rotating mirror
Recording medium	35 mm film, ASA 3200, 100 lps/mm
Recording lens	$f = 100\,\mathrm{mm}$, $f_\# = 2.8$
Illumination	Nd:YAG laser[a] 70 mJ/pulse
Pulse delay	$\Delta t = 2 - 4\,\mu\mathrm{s}$
Seeding material	oil droplets ($d_\mathrm{p} \approx 1\,\mu\mathrm{m}$)

[a] frequency doubled

The first two experiments were carried out in the DLR high-speed blow-down wind tunnel (HKG). Transonic flow velocities are obtained by sucking air from an atmospheric intake into a large vacuum tank. A quick-acting valve, located downstream of the test section, is rapidly opened to start the flow. Ambient air, which is dried before entering the test chamber, flows for a maximum of 20 s through a test section with 725 mm spanwise extension. Grids in the settling chamber and a high contraction ratio lead to a low turbulence level in the test section.

9.3.1 Cascade Blade with Cooling Air Ejection

The aim of this investigation was to study the effect of the ejection of cooling air on the wake behind a model of a cascade blade. Due to a specially adapted wind tunnel wall above and below the model and an adjustable tailboard above the model, the flow field of a real turbine blade could be simulated in a realistic manner. The PIV recordings were taken with the photo-graphical PIV recording system utilizing the high-speed rotating mirror for image shifting at a time delay between the two laser pulses of $2-4\,\mu$s. The PIV parameters used for this investigation are listed in table 9.7. Figure 9.12 presents the instantaneous flow velocity field at the trailing edge of the plate (thickness 2 cm) for a cooling mass flow rate of 1.4% at a free stream Mach number of $Ma = 1.27$. Expansion waves and terminating shocks can be easily seen. No data were obtained in the area above the model as the laser light was blocked off by the model. Data drop-out was also found in the area directly downstream of the model. The reason is mainly that the size of the interrogation area could not be further decreased at evaluation. This would have been necessary in order to satisfactorily resolve the strong velocity gradients close to the trailing edge

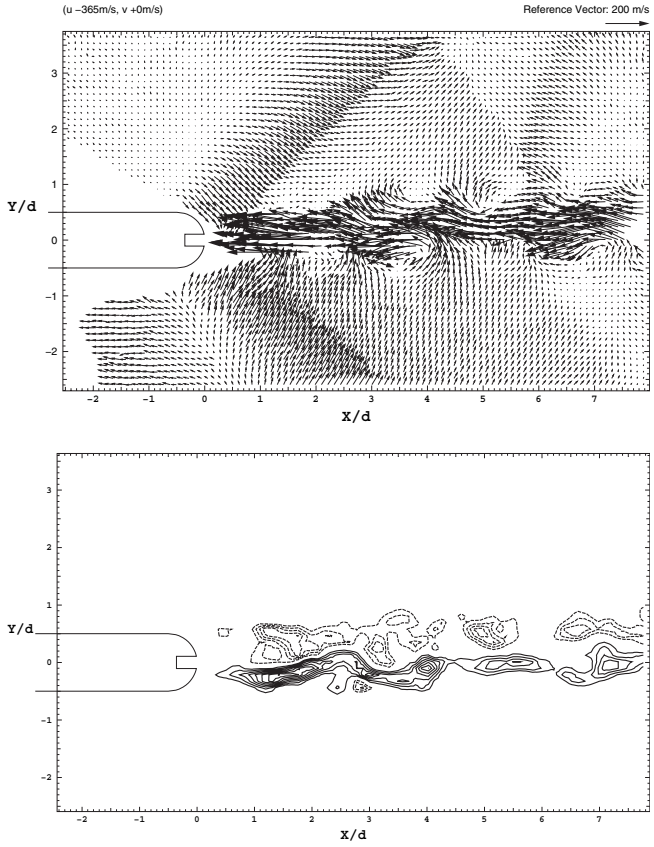

Fig. 9.12. Flow velocity (top) and vorticity field (bottom) behind a cascade blade at $Ma = 1.27$ and a cooling mass flow rate of 1.4%.

of the model. In addition, strong density gradients in this part of the flow field caused much broader particle images. Without ejection of cooling air, the wake behind the plate can be characterized as a vortex street [310]. With ejection of air this is no longer true: two separate thin shear layers can be detected in the presentation of the instantaneous vorticity shown in figure 9.12.

9.3.2 Transonic Flow Above an Airfoil

The application of PIV in high-speed flows yields two additional problems: the resulting behavior of the tracer particles and the presence of strong velocity gradients.

For the proper understanding of the velocity maps it is important to know how far behind a shock will the tracer particles again move with the velocity of the surrounding fluid. Experience shows that a good compromise between

Table 9.8. PIV recording parameters for transonic flow above a NACA0012 airfoil.

Flow geometry	$Ma = 0.75$ parallel to light sheet
Maximum in-plane velocity	$U_{\max} \approx 520\,\mathrm{m/s}$
Field of view	$300 \times 200\,\mathrm{mm}^2$
Interrogation volume	$5.6 \times 5.6 \times 1\,\mathrm{mm}^3$ $(H \times W \times D)$
Dynamic spatial range	DSR $\approx 57 : 1$
Dynamic velocity range	DVR $\approx 150 : 1$
Observation distance	$z_0 \approx 1\,\mathrm{m}$
Recording method	single frame/double exposure
Ambiguity removal	image shifting/rotating mirror
Recording medium	35 mm film, ASA 3200, 100 lps/mm
Recording lens	$f = 100\,\mathrm{mm}$, $f_\# = 2.8$
Illumination	Nd:YAG laser[a] 70 mJ/pulse
Pulse delay	$\Delta t = 3\,\mu\mathrm{s}$
Seeding material	oil droplets ($d_\mathrm{p} \approx 1\,\mu\mathrm{m}$)

[a] frequency doubled

particle behavior and light scattering can be found if this distance is allowed to be of the order of one or two interrogation areas.

Strong velocity gradients in the flow will lead to a variation of the displacement of the images of the tracer particles within the interrogation area. This influence can be reduced by application of image shifting, that is by decreasing the temporal separation between the two illumination pulses and increasing the displacement between the images of the tracer particles by image shifting to the optimum for evaluation. This is especially important if autocorrelation and optical evaluation methods are applied as in this case it is required to be able to adjust the displacement of the tracer particles to the range for optimal evaluation (i.e. $\approx 200\,\mu\mathrm{m}$). The PIV parameters used for this investigation are listed in table 9.8.

In the case of optical evaluation methods image shifting helps also to solve the problem of large variations of the displacements of the tracer particle images within the PIV recording. A successful evaluation is achieved for a range of particle image displacements of $150\,\mu\mathrm{m} \leq d_\mathrm{opt} \leq 250\,\mu\mathrm{m}$. The upper and lower limits for this optimal particle image displacement is determined by the flow to be investigated and can be adapted to the optimal range of displacement on the recording medium by applying the image shifting technique, and adding an additional shift in the direction of the mean flow. Less data drop-out can be expected by this means.

Strong velocity gradients are present in flow fields containing shocks as are present in transonic wind tunnels. Figure 9.13 shows such an instantaneous flow field – again above a NACA 0012 airfoil with a chord length of $C_l = 20\,\mathrm{cm}$ – at $Ma_\infty = 0.75$ [103]. By subtracting the speed of sound from all velocity vectors the supersonic flow regime and the shock are clearly detectable. Due

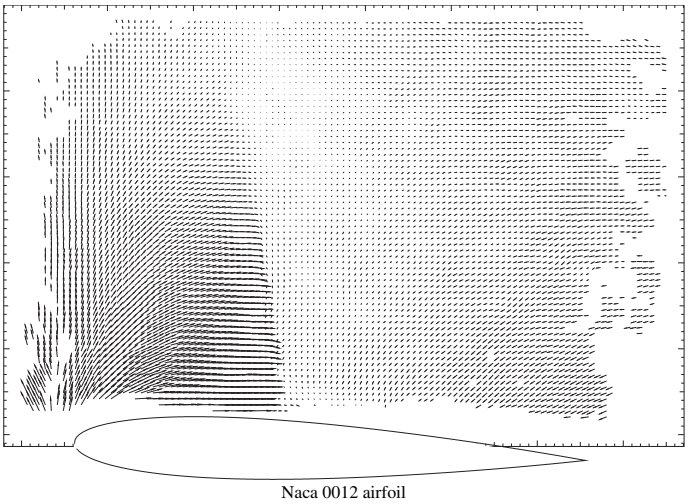

Fig. 9.13. Instantaneous flow field over a NACA 0012 airfoil at $\alpha = 5°$ and $Ma_\infty = 0.75$, $U_{\text{shift}} = 174\,\text{m/s}$, $C_l = 20\,\text{cm}$.

to the application of image shifting ($U_{\text{shift}} = 174\,\text{m/s}$) the requirement for the fluctuations to be less or equal to the particle image diameter could be fulfilled with an optimum interrogation spot diameter of 0.7 mm even at the location of the shock. No data drop-out is found even in interrogation spots located in front and behind the shock (flow velocities from $U = 280\,\text{m/s}$ to $520\,\text{m/s}$). The associated parameters for the PIV recording are presented in table 9.9.

The previous two examples should demonstrate, that already a decade ago the physical problems associated with the application of PIV in transonic flows could be tackled with some experimental effort even for photographic recording. To date, many of these problems have been solved in a more general way, for example using frame straddling enabling pulse delays of the laser of much less than $1\,\mu$s (optimal displacement of particle images). Furthermore, sophisticated evaluation algorithms providing high local resolution even in presence of strong displacement gradients and much stronger pulse lasers providing much higher intensities allow for either larger observation areas or a smaller

Table 9.9. Image recording parameters associated with the instantaneous flow field of figure 9.13.

$M = 1:6.7$		$N \approx 15$					
	U_{min} [m/s]	U_{max} [m/s]	Δt [μs]	U_{shift} [m/s]	ΔX_{shift} [μm]	ΔX_{min} [μm]	ΔX_{max} [μm]
without I.S.	200	520	5	0	0	149	388
with I.S.			3	174	78	167	311

aperture leading to sharp particle images even in case of strong vibrations of the wind tunnel and the PIV setup.

9.3.3 Shock Wave/Turbulent Boundary Layer Interaction

Contributed by:

F. Scarano, R.A. Humble, B.W. van Oudheusden

The interaction between an oblique shock wave and a turbulent boundary layer (SWTBLI) creates a series of complicated flow phenomena, such as unsteady flow separation and shock/turbulence interaction that present unique experimental challenges [307], [313] and [314]. The application of PIV in the supersonic flow regime presents the specific challenges of describing the high-speed flow in the presence of shock waves with sufficient accuracy, necessitating the quantitative evaluation of the tracer particle's dynamic behavior [312]. The SWTBLI problem additionally requires the large velocity gradient close to the wall and the high-frequency turbulent fluctuations to be resolved. The PIV parameters used for this investigation are listed in table 9.10.

The particle tracer relaxation time/length is a crucial parameter dictating the spatio-temporal resolution of the measurement. It is directly evaluated by measuring the particle velocity profile across a planar steady shock wave. Figure 9.14 shows the normal velocity profile against the shock-normal abscissa s, and returns a particle relaxation time of $\tau_\mathrm{p} = 2.1\,\mu$s. The

Table 9.10. PIV recording parameters for shock wave/turbulent boundary layer interaction on a flat plate (second set denotes parameters for boundary layer study.)

Flow geometry	parallel to light sheet
Maximum in-plane velocity	$U_\mathrm{max} \approx 500\,\mathrm{m/s}$ (Ma = 2.1)
Field of view	$124 \times 39\,\mathrm{mm}^2$ ($16 \times 5\,\mathrm{mm}^2$) ($W \times H$)
Interrogation volume	$1.9 \times 1.9 \times 1.5\,\mathrm{mm}^3$ ($0.7 \times 0.08 \times 1.5\,\mathrm{mm}^3$)
Dynamic spatial range	DSR $\approx 136:1$
Dynamic velocity range	DVR $\approx 400:1$
Observation distance	$z_0 \approx 600\,\mathrm{mm}$ ($z_0 \approx 150\,\mathrm{mm}$)
Recording method	dual frame/single exposure
Ambiguity removal	frame separation (frame-straddling)
Recording medium	full frame interline transfer CCD 1376×1040 (432 active) pixels
Recording lens	$f = 60\,\mathrm{mm}$, $f_\# = 8$ ($f = 105\,\mathrm{mm}$, $f_\# = 8$)
Illumination	Freq. doubled Nd:YAG laser, 400 mJ/pulse at 532 nm
Pulse delay	$\Delta t = 2\,\mu$s ($0.6\,\mu$s)
Seeding material	TiO_2 ($d_\mathrm{p} \approx 400\,\mathrm{nm}$)

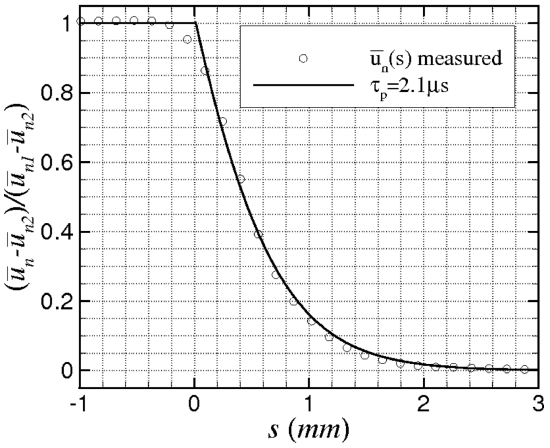

Fig. 9.14. Normal velocity profile against shock-normal abscissa s.

corresponding frequency response is $f_\mathrm{p} \approx 0.5\,\mathrm{MHz}$. The Stokes number $St = \tau_\mathrm{p}/\tau_\mathrm{flow}$ ($\tau_\mathrm{flow} = \delta/U_\infty$) expresses the fidelity of particle tracers in the specific flow experiment [311]. For the present case $St = 0.06$, yielding an RMS tracking error below 1%.

The flow statistical properties are evaluated on the basis of 500 PIV recordings acquired at 10 Hz in a supersonic wind tunnel of $270(H) \times 280(W)\,\mathrm{mm}^2$ test section. The upstream mean boundary layer profile ($\delta_{99} = 20\,\mathrm{mm}$, $\mathrm{Re}_\theta = 3.36 \times 10^4$) scaled with inner variables is shown in figure 9.15. The experimental data agree with the composite formula down to $y^+ \approx 200$. When the evaluation is carried out using high-aspect ratio interrogation windows (61×7 pixels) the wall-normal spatial resolution is improved extending the agreement to the overlap region ($y^+ \approx 80$, $y < 0.2\,\mathrm{mm}$).

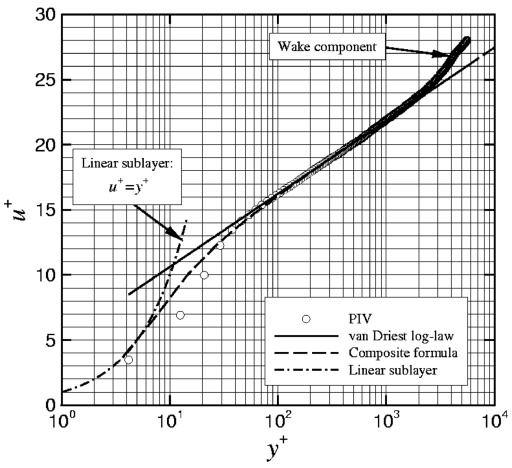

Fig. 9.15. Upstream mean boundary layer velocity profile.

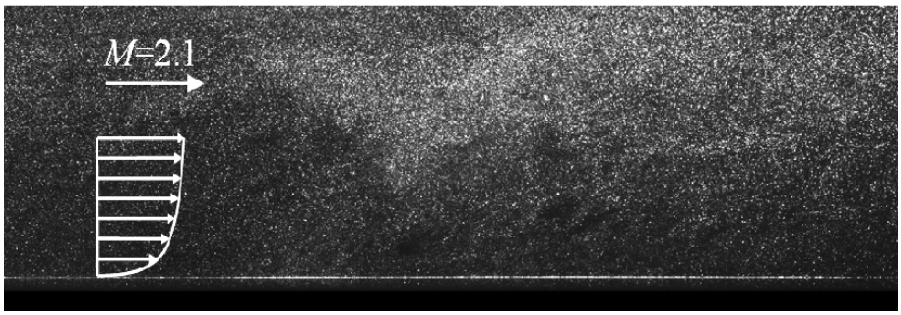

Fig. 9.16. Single PIV recording with mean velocity profile.

The instantaneous recording depicted in figure 9.16 shows a non-uniform seeding particle concentration due to the density variation in the flow. The incident and reflected shock waves can be visualized by the increase in tracer particle density, whilst the boundary layer is highlighted by a comparatively lower seeding level. Laser light reflections from the wall were minimized during the experiment by illuminating almost tangent to the wall.

An instantaneous stream-wise velocity distribution is shown in figure 9.17 (top). The incoming boundary layer has a clear intermittent nature. The global structure of the interaction is formed by the impinging shock penetrating the boundary layer, turning and weakening until it vanishes at the sonic line. The adverse pressure gradient generated by the shock causes a dilation of the subsonic layer, which causes a second compression wave system to emanate upstream of the impinging shock. The irregular shape of the separated region exhibits turbulent coherent structures, mostly originating from the separated shear layer instability. Downstream of the interaction these structures enhance the momentum mixing, which drives the boundary layer recovery.

The mean flow behavior is described by the averaged velocity field in figure 9.17 (middle). The incident and reflected shock waves are visible as a sharp flow deceleration and change of direction for the first, whereas the reflected shock exhibits a smoother spatial variation of the velocity due to its unsteady nature and the averaging effect. An inflection point prior to separation is visible in the boundary layer profile. However, from the mean velocity vector profiles no reverse flow can be inferred. After reattachment, the distorted boundary layer has approximately doubled its thickness and develops downstream with a relatively low rate of recovery.

The spatial distribution of the turbulence intensity magnitude $(\overline{u}'^2 + \overline{v}'^2)^{1/2}/U_\infty$ is depicted in figure 9.17 (bottom) and shows the turbulent properties of the incoming boundary layer, the increased level of fluctuations throughout the interaction region and its redevelopment downstream. The higher level of fluctuations associated to the impinging shock (approximately 4%) is typically encountered in these experimental conditions and is ascribed to the combined effect of the decreased measurement precision and

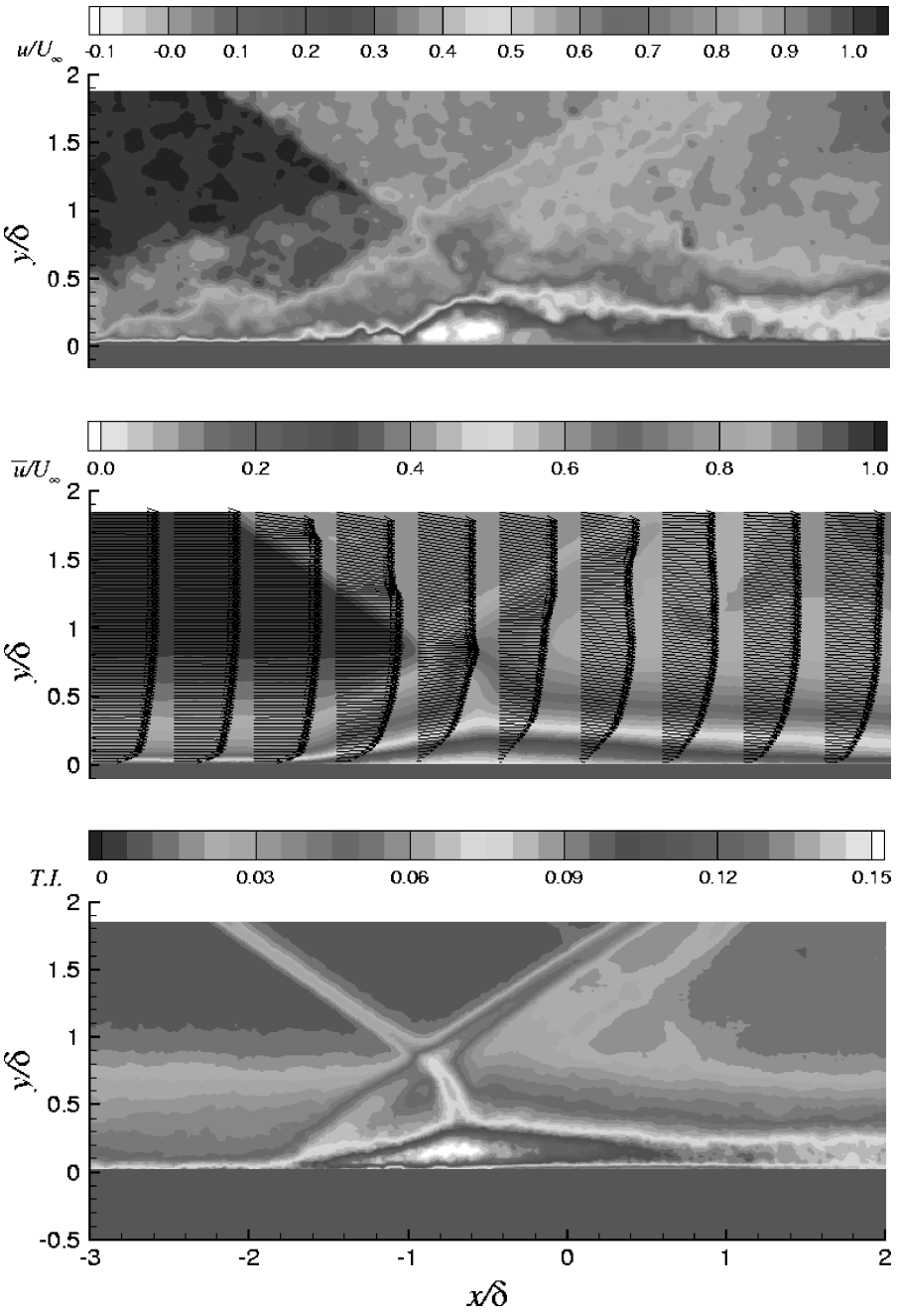

Fig. 9.17. Instantaneous stream-wise velocity distribution (top), mean velocity vector field (middle) and turbulence intensity magnitude (bottom).

to small fluctuations of the shock position. The increased level of fluctuations associated with the impinging shock penetrating the boundary layer is due to its interaction with turbulent coherent structures convected in this region. The reflected shock exhibits a clear unsteady behavior and relatively high levels of fluctuation, which in this case should not be regarded as turbulence. Two weak features downstream of the reflected shock (one parallel and the other roughly perpendicular to it) are due to optical aberration effects introduced by the inhomogeneous index of refraction field of this compressible flow [308].